Computation of Mössbauer isomer shifts from first principles

2009 J. Phys.: Condens. Matter 21 195501

(http://iopscience.iop.org/0953-8984/21/19/195501)

IOP PUBLISHING JOURNAL OF PHYSICS: CONDENSED MATTER

J. Phys.: Condens. Matter **21** (2009) 195501 (6pp) doi:10.1088/0953-8984/21/19/195501

Computation of Mössbauer isomer shifts from first principles

J W Zwanziger

Department of Chemistry and Institute for Research in Materials, Dalhousie University, Halifax, NS, B3H 4J3, Canada

E-mail: jzwanzig@dal.ca

Received 22 February 2009, in final form 12 March 2009
Published 7 April 2009
Online at stacks.iop.org/JPhysCM/21/195501

Abstract

Computation of the observables of a Mössbauer spectrum, primarily the isomer shift, from a first-principles approach is described. The framework used is density functional theory using the projector augmented wave formalism (DFT PAW), which enables efficient computation even of many-electron solids such as $SnCl_2$. The proper PAW version of the isomer shift is derived and shown to be correct through comparison of computed shifts and experiment in a variety of compounds based on tin, germanium and zinc. The effects of pressure are considered as well as motional effects including the Lamb–Mössbauer factor and the second-order Doppler shift.

1. Introduction

Mössbauer spectra reflect the electronic and crystallographic structure of materials through several observables, including the isomer shift and the electric field gradient [1, 2]. The isomer shift is due to both nuclear factors and the difference in the electron density at the probed nucleus in the source and the absorber. In comparing a range of materials by way of the same nuclear transition, the nuclear factors are constant and the isomer shift can be described in a relative way just through the electron density. The electric field gradient affects the Mössbauer spectrum due to coupling to the electric quadrupole moments of the probed nucleus, which are again constant for a given nuclear transition. The electric field gradient itself arises from the distribution of charges in the neighbourhood of the nucleus, both electronic and ionic. Computing and interpreting Mössbauer spectra thus becomes in large part a problem of computing the electron density and the electric field gradient at the probe nucleus. From these two results the spectrum can be reconstructed if the nuclear parameters are known, and in any case different materials can be compared in terms of relative shifts and couplings.

Computational quantum mechanics provides many schemes for computing the electron density and electric field gradient, including wavefunction-based methods in real space and reciprocal space, and density functional methods also in real space and reciprocal space [3–12]. One highly accurate method involves computing the wavefunctions of a molecule or cluster model of a solid using all-electron real-space methods [4, 8, 9]. In this method as applied to solids, however, it is necessary to find ways of truncating the solid accurately, and it is also difficult to consider perturbations due to mechanical and electromagnetic fields, and to long-range magnetic ordering. For solid compounds treated with periodic boundary conditions, the most accurate method is the full-potential linearized augmented plane wave (LAPW) treatment [8–10, 12], which is again an all-electron method. This is a highly accurate method but it is also computationally expensive, and so it is of interest to investigate whether it is possible using a pseudopotential or related method to achieve comparable accuracy in solids with periodic boundary conditions at lower computational cost. Because pseudopotential methods treat only the valence electrons explicitly, it is also interesting to study whether this level of treatment is at all capable of computing local nuclear effects such as the isomer shift with sufficient accuracy. In fact, perhaps surprisingly, it has already been shown that the magnetic chemical shielding [13–15] and electric field gradient [16, 17] can be accurately treated with pseudopotential methods, provided that the projector augmented wave method is used to reconstruct the all-electron expectation values in the valence space. The core electrons are still treated with pseudized functions in this approach.

Thus, the purpose of the present contribution is to describe the computation of Mössbauer observables, in particular the isomer shift, using a scheme based on density functional theory and the projector augmented wave formalism (PAW). This method recovers all-electron accuracy in the valence space at a computational efficiency similar to ultrasoft pseudopotential schemes. The PAW data can be constructed with relativistic

corrections, and the scheme presented below is compatible with a variety of electronic structures: metals and insulators, magnetic order, strong on-site electron correlation, and so forth. We describe the implementation in PAW first and then present a variety of examples using it to compute Mössbauer observables in tin, germanium and zinc. Special attention is paid to the effects of pressure and to nuclear motion, in the form of the Lamb–Mössbauer factor and the second-order Doppler shift.

2. Theoretical methods

The projector augmented wave method (PAW [18–20]) defines a linear operator T that acts on pseudowavefunctions $|\tilde{\Psi}\rangle$ and recovers all-electron wavefunctions $|\Psi\rangle$:

$$|\Psi\rangle = T|\tilde{\Psi}\rangle, \tag{1}$$

where

$$T = \mathbf{1} + \sum_i (|\Phi_i\rangle - |\tilde{\Phi}_i\rangle)\langle\tilde{p}_i|. \tag{2}$$

Here $|\Phi_i\rangle$ and $|\tilde{\Phi}_i\rangle$ represent, respectively, all-electron and pseudopartial waves describing the valence electrons at a given atom, within a defined cutoff radius. Outside this radius the two descriptions agree exactly by construction. The projector functions $|\tilde{p}_i\rangle$ are dual to the $|\tilde{\Phi}_i\rangle$. The cutoff radii are chosen large enough that the projectors are smooth and all functions can be expanded with a low-energy plane wave basis set, but not so large that neighbouring spheres overlap. The advantage of this formalism is that all-electron accuracy in the valence space is recovered within a calculation framework similar in efficiency to ultrasoft pseudopotentials. We will use this method as implemented in the `abinit` code in the studies below [20, 21].

For an observable A, equation (1) above provides a definition of a pseudo-operator $\tilde{A}$ through

$$\langle\Psi|A|\Psi\rangle = \langle\tilde{\Psi}|\tilde{A}|\tilde{\Psi}\rangle. \tag{3}$$

For a local or semi-local observable A and a complete set of partial waves $|\Phi\rangle$ and $|\tilde{\Phi}\rangle$, one can show that

$$\tilde{A} = A + \sum_{ij} |\tilde{p}_i\rangle(\langle\Phi_i|A|\Phi_j\rangle - \langle\tilde{\Phi}_i|A|\tilde{\Phi}_j\rangle)\langle\tilde{p}_j|. \tag{4}$$

These two equations are critical because they provide a path to calculate the all-electron expectation value of the observable (the left-hand side of equation (3)) in terms of the pseudowavefunctions that are computed by a pseudopotential-based DFT code (the right-hand side of equation (3)).

In Mössbauer spectroscopy, two of the key observables are the quadrupole coupling and the isomer shift. The quadrupole coupling arises from an interaction between the nuclear electric quadrupole moment and the electric field gradient at the nuclear site. The electric field gradient may be computed within the PAW method with excellent accuracy on metals, semiconductors and insulators, and the methods of implementation have been published and tested [16, 17]. The isomer shift depends on the electronic wavefunction density at the nuclear site of both the absorber and source, and is expressed in velocity units as

$$\delta = \frac{c}{E_\gamma}\frac{2\pi Ze^2}{3}(|\Psi(0)_{\mathrm{A}}|^2 - |\Psi(0)_{\mathrm{S}}|^2)\Delta\langle r^2\rangle. \tag{5}$$

Here c is the speed of light, E_γ the γ-ray energy, Z the atomic number, e the electron charge and $\Delta\langle r^2\rangle$ the change in the mean square nuclear radius for the transition. The electronic densities $|\Psi(0)_{\mathrm{A}}|^2$ and $|\Psi(0)_{\mathrm{S}}|^2$ refer to the absorber and source, respectively.

Within the PAW formalism we identify the observable of interest for the isomer shift as $A = \delta(\mathbf{R})$, that is, the Dirac delta function evaluated at a nuclear site $\mathbf{R}$. That will certainly yield the electronic density $|\Psi|^2$ evaluated precisely at the nuclear point. In order to evaluate the matrix elements of A in equation (4), it is necessary to specify the form of the partial waves Φ and $\tilde{\Phi}$; these are constructed as [20]

$$\Phi_i(\mathbf{r}) = \frac{u_{n_i,l_i}(r)}{r} S_{l_i,m_i}(\hat{r}), \tag{6}$$

$$\tilde{\Phi}_i(\mathbf{r}) = \frac{\tilde{u}_{n_i,l_i}(r)}{r} S_{l_i,m_i}(\hat{r}), \tag{7}$$

that is, as atomic-like orbitals with radial components u_{nl}/r and angular components given by (real) spherical harmonics S_{lm}, centred at $\mathbf{R}$ as the origin. Matrix elements are then evaluated as

$$\begin{aligned}\langle\Phi_i|\delta(\mathbf{r})|\Phi_j\rangle &= \int \frac{u_{n_i,l_i}}{r}\frac{u_{n_j,l_j}}{r} S_{l_i,m_i} S_{l_j,m_j} \\ &\quad \times \frac{\delta(r)}{4\pi r^2} r^2 \sin\theta \,\mathrm{d}r\,\mathrm{d}\theta\,\mathrm{d}\phi \\ &= \frac{1}{4\pi}\delta_{l_i,l_j}\delta_{m_i,m_j}\int \frac{u_{n_i,l_i}u_{n_j,l_j}}{r^2}\delta(r)\,\mathrm{d}r,\end{aligned} \tag{8}$$

where we have expressed the δ function in spherical coordinates as

$$\delta(\mathbf{r}) = \frac{\delta(r)}{4\pi r^2}. \tag{9}$$

Equation (8) shows that the desired result is

$$\frac{1}{4\pi}\delta_{l_i,l_j}\delta_{m_i,m_j}\lim_{r\to 0}\frac{u_{n_i,l_i}u_{n_j,l_j}}{r^2}. \tag{10}$$

The limit is unstable numerically because of the denominator. However, this problem is avoided by using L'Hôspital's theorem, which applies because the u functions in the numerator also go to zero at the origin. In fact applying the theorem twice yields

$$\lim_{r\to 0}\frac{u_{n_i,l_i}u_{n_j,l_j}}{r^2} = u'_{n_i,l_i}(0)u'_{n_j,l_j}(0), \tag{11}$$

where $u'(r) = \mathrm{d}u(r)/\mathrm{d}r$. The limiting slopes of the u functions can be computed very stably from their first few points, and in this way various extrapolations and numerical differentiations are avoided.

Two additional simplifications are also used. First, because of the dependence of the result on the slopes of the u functions at $r = 0$, only s-type partial waves contribute. Second, because the observable of interest is strictly localized

within the PAW spheres, in the limit of a complete set of partial waves the contribution to $\langle\Psi|A|\Psi\rangle = \langle\tilde{\Psi}|\tilde{A}|\tilde{\Psi}\rangle$ from the term $\langle\tilde{\Psi}|A|\tilde{\Psi}\rangle$ in equation (4) will be exactly cancelled by the last term involving the matrix elements using $|\tilde{\Phi}\rangle$. Therefore, the *only* terms necessary to compute are

$$\sum_{ij}\langle\tilde{\Psi}|\tilde{p}_i\rangle\langle\Phi_i|\delta(\mathbf{R})|\Phi_j\rangle\langle\tilde{p}_j|\tilde{\Psi}\rangle$$
$$= \frac{1}{4\pi}\sum_{ij,l_i=l_j=0}\rho_{ij}u'_{n_i,l_i}(0)u'_{n_j,l_j}(0) \qquad (12)$$

where $\rho_{ij} = \langle\tilde{\Psi}|\tilde{p}_i\rangle\langle\tilde{p}_j|\tilde{\Psi}\rangle$. The terms ρ_{ij} represent the electron occupation of the ij pair of atomic functions, and are computed as part of the self-consistency cycle. These factors represent the details of the electronic configuration of a given material and can be fractional, in the case of metals, and can have different values for different spin densities, in the case of magnetism. From the computational perspective of the present work, they are simply obtained in the minimization of the total energy functional and are then combined as above to compute the observables.

The above method, equation (12), for computing the isomer shift (more accurately, the Fermi contact interaction) was implemented in the `abinit` software package. As noted above, this package can perform density functional theory calculations on solids using the PAW formalism. As implemented it is compatible with variable band occupation numbers (insulators and metals), variable numbers of spin densities and variable numbers of spinor wavefunctions. Therefore one can study magnetic materials and spin–orbit coupled systems in addition to simple metals and insulators.

The PAW atomic datasets used in this study were constructed using the `atompaw` code [22], which has been adapted for use with `abinit`. All sets used two projectors per angular momentum channel and were made using a scalar relativistic Schrödinger equation and the Perdew–Burke–Ernzerhof (PBE) generalized gradient approximation exchange and correlation functions [23]. PAW radii of 2.0–2.3 Bohr were used, depending on the atom. In the case of the main group elements studied here (tin and germanium), semi-core d electrons were included in the valence space in addition to s and p, leading in each case to 14 valence electrons. The zinc set used a similar complement of s, p and d channels. In the solid-state calculations, all properties of interest (energy, stress, Fermi contact, quadrupole couplings) converged to parts in 10 000 or better (much better in the case of energy) at the plane wave cutoff level of 15 Hartree (about 400 eV). In each case reciprocal space was sampled using Monkhorst–Pack grids [24] at a density of 0.04 Å^{-1} or better.

3. Results and discussion

3.1. Tin-119 isomer shifts

Tin-119 Mössbauer spectra provide a relatively simple test suite for the theory outlined above, because there are many examples in the literature with good resolution, there is a relatively large range in isomer shifts and the solids are not subject to complicating magnetic or strong electron correlation effects. Figure 1 shows the correlation between experimentally determined isomer shifts and the valence electron density at the tin nucleus as computed with the scheme discussed above. Note in the figure that the valence densities are plotted; to get the absolute total calculated density, to each would be added the identical term arising from the core density, which can be obtained in the construction of the PAW datasets. In the PAW method, as in other pseudopotential methods, the core density is fixed at the construction of the pseudopotential and is then identical in all applications. In the present case, this value is $418\,554 e/a_0^3$. Of more importance is the change in the densities; from equation (5) the slope of the experimental shift as a function of electron density should be given by $(c/E_\gamma)(2\pi Ze^2/3)\Delta\langle r^2\rangle$, where the core densities of the absorbers and the total density of the source both appear in the intercept, being constant values. For ^{119}Sn, $Z = 50$ and $E_\gamma = 23.875$ keV, and so from the slope in figure 1 we can extract the value $\Delta\langle r^2\rangle = 4.79 \times 10^{-3}$ fm^2. Using this figure, other samples can be computed and their velocity shifts calculated for direct comparison with experiment. Moreover, the figure for $\Delta\langle r^2\rangle$ we obtain is in reasonable agreement with other derived values, for example 6–7 $\times 10^{-3}$ fm^2 [7, 11] from linear muffin-tin orbital calculations.

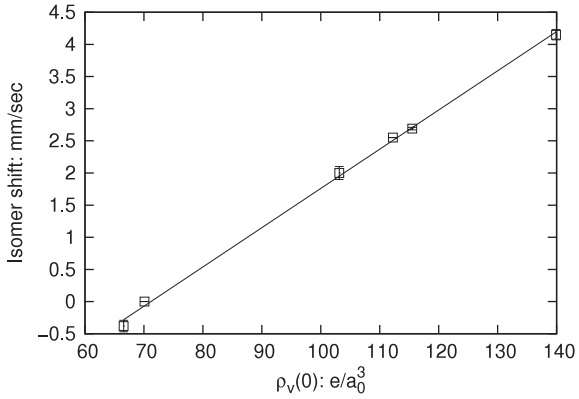

Figure 1. Correlation of experimental ^{119}Sn shifts with computed valence densities. Data from the Mössbauer Effect Data Center (http://orgs.unca.edu/medc/index.html) referenced to the shift of $^{119}SnO_2$. Compounds represented from the smallest shift to the largest are SnF_4, SnO_2, α-Sn, β-Sn, SnO and $SnCl_2$. The computed values are expressed in units of electrons per cubic Bohr.

3.2. Germanium-73 isomer shifts

Germanium-73 isomer shifts are not as well defined experimentally as are tin shifts. Figure 2 shows the correlation between the valence electron density and the measured shifts, referenced to bulk germanium. Several experimental determinations of some of the compounds are shown, along with their associated errors. For ^{73}Ge, with $Z = 32$ and $E_\gamma = 13.3$ keV, we obtain from the slope of figure 2 the estimate $\Delta\langle r^2\rangle = 9.1 \times 10^{-3}$ fm^2. From this value, as above, computations of other Ge-containing samples may be compared directly to experiment.

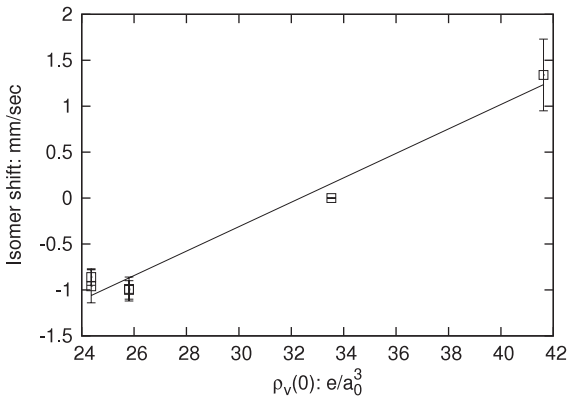

Figure 2. Correlation of computed valence densities with measured ^{73}Ge isomer shifts. Compounds represented from the smallest shift to the largest are hexagonal GeO_2, rutile GeO_2, Ge and GeSe. The computed values are expressed in units of electrons per cubic Bohr. Data from [25, 26].

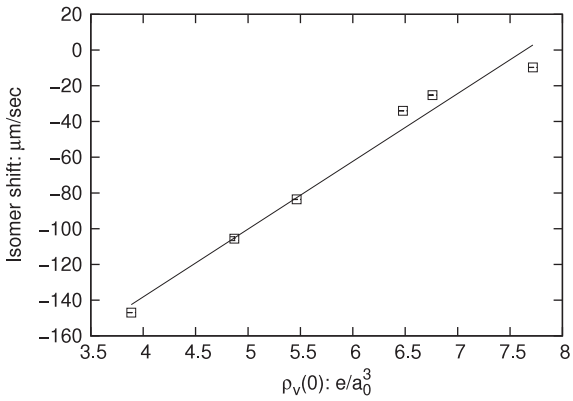

Figure 3. Correlation of experimental ^{67}Zn shifts corrected for the second-order Doppler shift with computed valence electron densities. Shift data from [27]; computed second-order Doppler shifts and valence densities as described in the text and table 1.

Table 1. Experimental ^{67}Zn Mössbauer shifts from [27], and calculated valence electron densities, second-order Doppler shifts (S_D) and Lamb–Mössbauer factors (LMF). The valence densities are computed with the PAW scheme using the experimental crystal structures. The S_D and LMFs are derived from computed phonon dispersion curves, using density functional perturbation theory. Both factors are computed at a temperature of 4.2 K. Only isotropic values are reported.

Compound	Expt. shift (μm s^{-1})	$\rho_v(0)$	S_D (μm s^{-1})	LMF (%)
ZnF_2	−174.1	3.925	−27.1	1.56
c-ZnO	−130.7	4.869	−25.1	1.67
h-ZnO	−110.7	5.464	−27.1	1.65
c-ZnS	−56.5	6.479	−22.5	0.67
c-ZnSe	−47.0	6.760	−21.8	0.50
c-ZnTe	−30.7	7.718	−21.0	0.38

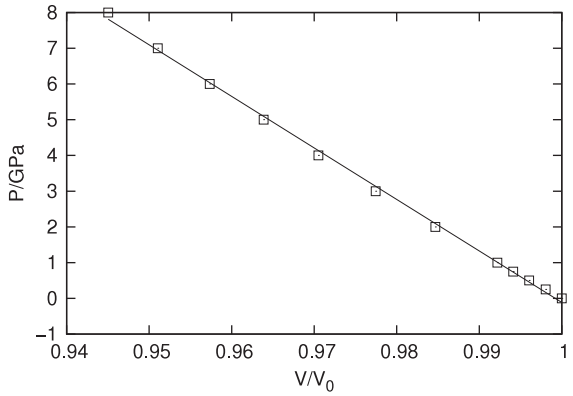

Figure 4. Calculated pressure–volume relationship for wurtzite structured ZnO. The cell volume is scaled to the value at zero pressure. At each target pressure the cell and ion positions were relaxed, allowing for anisotropic contraction while maintaining the space group symmetry.

3.3. Zinc-67 isomer shifts

Unlike ^{119}Sn and ^{73}Ge, ^{67}Zn displays a very small isomer shift range, and the low recoil-free fraction requires that the experiments be done at very low temperatures. In addition, theoretical interpretation of the shifts requires consideration of the second-order Doppler effect, due to the extreme sharpness of the transition.

We have computed the valence density at zinc in a variety of compounds, see table 1. In order to compare the calculations to experiment, it is necessary as mentioned to take the second-order Doppler effect into account. This term, as is well known, is expressed in velocity units by

$$S_D = -\frac{1}{2c}\langle v^2 \rangle, \tag{13}$$

where c is the speed of light and $\langle v^2 \rangle$ is the mean square velocity of the Mössbauer atom (zinc in the present case). We computed S_D by a first-principles method, using density functional perturbation theory as implemented in the `abinit` package to calculate the phonon dispersion curves [28, 29]. Then, from this information and the phonon eigenvectors, the mean square velocities were determined. For completeness we also calculated the Lamb–Mössbauer factors, which are related to the mean square displacements of the atoms and the photon wavevector.

The isomer shifts can be extracted from the experimental shifts by subtracting the S_D contribution as estimated above. The shifts so constructed are correlated with our calculated valence densities in figure 3. From the slope of this graph and equation (5), the term $\Delta\langle r^2 \rangle$ may be determined again as a consistency check of the computational scheme. Using parameters for ^{67}Zn ($Z = 30$ and $E_\gamma = 93.31$ keV) we determine $\Delta\langle r^2 \rangle = (19.5 \pm 1.6) \times 10^{-3}$ fm^2, in close agreement with the experimentally determined one of $(18 \pm 4) \times 10^{-3}$ fm^2 [30].

The case of hexagonal ZnO is particularly interesting because it undergoes a transition to a cubic structure at about 11 GPa. This transition has been studied extensively, by diffraction experiments [31] and by Mössbauer spectroscopy [32]. We have studied this compound in the low pressure regime. The calculated pressure–volume relationship is shown in figure 4. Figures 5 and 6 show, respectively, the valence density change and electric field gradient coupling

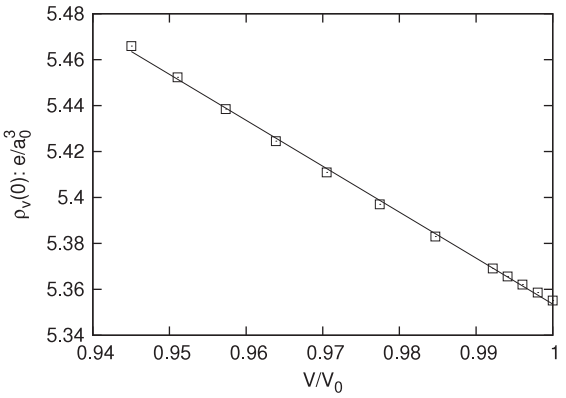

Figure 5. Dependence of calculated valence electron density as a function of cell volume, scaled to ambient pressure, in wurtzite structured ZnO. The results shown here are for the relaxed structures.

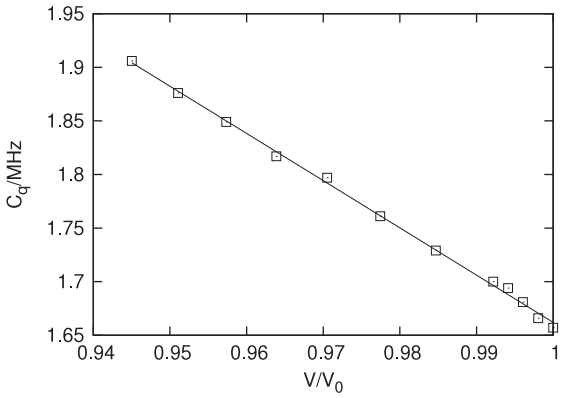

Figure 6. Dependence of calculated electric field gradient coupling in MHz as a function of cell volume, scaled to ambient pressure, in wurtzite structured ZnO.

e^2qQ/h as a function of reduced cell volume. Note that these calculations were done by optimizing the cell structure and ion locations for a constant stress tensor describing the desired hydrostatic pressure; this methodology allows the cell to contract anisotropically. The plots are made as a function of cell volume simply to make comparison with literature reports easier.

The plot of pressure versus cell volume (figure 4) shows almost perfectly linear behaviour in this regime, and allows the modulus $B = -V_0(\partial P/\partial V)|_{V_0}$ to be derived. We find $B = 144.2 \pm 1.7$ GPa, in good agreement with several experimental measurements, which found 142.6 GPa [31] and 140 ± 2 GPa [33], but not in good agreement with the value found by Karzel *et al*, 204 ± 9 GPa [32].

Considering the electric field gradient, we find by using the experimental crystal structure [34, 35] the value 2.72 ± 0.27 MHz, where the uncertainty comes from the uncertainty in the ^{67}Zn electric quadrupole moment [36]. This value is in fair agreement with the Mössbauer result of 2.401 MHz. The case of ZnF_2 shows a similar level of agreement with experiment: 6.8 ± 0.7 MHz and asymmetry 0.22, compared to 7.92 ± 0.05 MHz and 0.29 ± 0.03 [8]. As the cell is relaxed, the computed value drops to 1.66 MHz, although the unit cell lengths only lengthen by about 2%, as is typical when using a generalized gradient functional such as PBE [23]. The value of the density at the Zn nucleus changes similarly; compare table 1, which shows the result for the experimental structure, with figure 5, which shows relaxed structures. Significantly, the ionic contribution to the electric field gradient hardly changes during the relaxation, essentially all the change occurs due to redistribution of electron density in different orbitals at the Zn site. This finding indicates a very high sensitivity of the chemical bonding in this compound to small structural changes. As a function of reduced cell volume we find the coupling to vary with a slope of -4.4 MHz, considerably less than the value reported from Mössbauer studies of -18.2 MHz [27]. Likewise, we find the valence density to change much more slowly with cell volume than literature reports, -2.00 ± 0.02 versus -10.7 ± 3.4 [27].

Given the success of the PAW method in computing the isomer shift and the electric field gradient (as measured by the above results for $\Delta\langle r^2\rangle$ in ^{119}Sn and ^{67}Zn, and various reports for electric field gradients [16, 17]), how can the sharp deviations for wurtzite ZnO be understood? We believe the key is in the extreme sensitivity of the bonding to local structural changes. In our calculations we use strictly the wurtzite structure, while the experimental work found that the quadrupole asymmetry η also increased sharply with pressure. This parameter is defined as

$$\eta = \frac{V_{xx} - V_{yy}}{V_{zz}}, \tag{14}$$

where V_{zz}, V_{yy} and V_{xx} are the principal components of the electric field gradient tensor ordered from largest to smallest in magnitude. Thus a non-zero value of η measures the deviation of the tensor from axial symmetry. However, in the hexagonal ZnO structure [34, 35], Zn lies on Wyckoff position 2b of space group $P6_3mc$, and this position lies on a threefold symmetry axis. Therefore, it is not possible to have a non-zero η for this site. Furthermore, as noted above, the bulk modulus determined using a similar pressure clamp as the Mössbauer measurements found a bulk modulus that is not in good agreement with other experimental determinations.

It would appear that in the Mössbauer experimental apparatus the pressure applied was not hydrostatic and broke the symmetry of the hexagonal crystal. Indeed, the spectrometer is described as having pressure gradients of less than 10%; we found that by applying strain along the crystal a axis sufficient to generate about a 10% differential in the resulting stress tensor elements (and of course also lowering the symmetry of the crystal), an electric field gradient asymmetry η of 0.22 was induced. Therefore, the lack of agreement between theory and experiment in this case is not a signature that the theory is deficient; rather, that they are describing two different situations: the computation is for the fully symmetric hexagonal structure, while the experiment evidently applied the pressure anisotropically and so generated a distorted crystal.

4. Conclusions

In this paper we have presented a formalism for computing the electronic density at the nucleus, which is proportional to the Mössbauer isomer shift, in a framework suitable for applications to solids. By using the projector augmented wave method, all-electron accuracy is recovered in the valence space, which is shown to be sufficient to model spectra in a variety of solids. Because the PAW datasets can be computed with relativistic terms, even heavy elements are accurately treated. Moreover, because of the flexibility of the implementation and the fact that it is constructed with periodic boundary conditions, the effects of mechanical perturbations as well as complex electronic and magnetic structures are easily treated. We showed applications in relatively simple cases, such as a range of tin, germanium and zinc solids, where good agreement with experimental shifts was obtained. In the case of hexagonal ZnO, we showed that previous experimental results using pressure probably included significant distortions due to anisotropic loading.

References

[1] Greenwood N N and Gibb T C 1971 *Mössbauer Spectroscopy* (London: Chapman and Hall)

[2] Long G J and Grandjean F (ed) 1993 *Mössbauer Spectroscopy Applied to Magnetism and Materials Science* (New York: Plenum)

[3] Shrivastava K N 1976 Mössbauer isomer shifts in $^{67}Zn^{++}$ and $^{61}Ni^{++}$ nuclei *Phys. Rev.* B **13** 2782–6

[4] Duff K J, Mishra K C and Das T P 1981 *Ab initio* determination of $^{57}Fe^{m}$ quadrupole moment from Mössbauer data *Phys. Rev. Lett.* **46** 1611–4

[5] Männing V and Grodzicki M 1986 Theoretical interpretation of Mössbauer spectra of tin-119 compounds *Theor. Chim. Acta* **70** 189–202

[6] Winkler W, Vetter R and Hartmann E 1987 Mössbauer isomer shift calibration of tin-119 using pseudopotential and $x\alpha$ SW calculations *Chem. Phys.* **114** 347–58

[7] Svane A and Antoncik E 1987 Theoretical investigation of the isomer shifts of the ^{119}Sn Mössbauer isotope *Phys. Rev.* B **35** 4611–24

[8] Steiner M *et al* 1994 Lattice dynamics and hyperfine interactions in ZnF_2 single crystals *Phys. Rev.* B **50** 13355–63

[9] Karzel H *et al* 1996 Lattice dynamics and hyperfine interactions in ZnO and ZnSe at high external pressures *Phys. Rev.* B **53** 11425–38

[10] Steiner M, Potzel W, Karzel H, Schiessl W, Köfferlein M, Kalvius G M and Blaha P 1996 Electronic topological transition in zinc metal at high external pressure *J. Phys.: Condens. Matter* **8** 3581–99

[11] Svane A, Christensen N E, Rodriguez C O and Methfessel M 1997 Calculations of hyperfine parameters in tin compounds *Phys. Rev.* B **55** 12572–7

[12] Lippens P E, Jumas J-C and Olivier-Fourcade J 2004 First principles calculations of Mössbauer spectra of intermetallic anodes for lithium-ion batteries *Hyperfine Interact.* **156/157** 327–33

[13] Pickard C J and Mauri F 2001 All-electron magnetic response with pseudopotentials: NMR chemical shifts *Phys. Rev.* B **63** 245101

[14] Yates J R, Pickard C J, Mauri F and Payne MC 2003 Relativistic nuclear magnetic resonance chemical shifts of heavy nuclei with pseudopotentials and the zeroth-order regular approximation *J. Chem. Phys.* **118** 5746–53

[15] Yates J R, Pickard C J and Mauri F 2007 Calculation of NMR chemical shifts for extended systems using ultrasoft pseudopotentials *Phys. Rev.* B **76** 024401

[16] Profeta M, Mauri F and Pickard C J 2003 Accurate first principles prediction of ^{17}O NMR parameters in SiO_2: assignment of the zeolite ferrierite spectrum *J. Am. Chem. Soc.* **125** 541

[17] Zwanziger J W and Torrent M 2008 First principles calculation of electric field gradients in metals, semiconductors and insulators *Appl. Magn. Reson.* **33** 447–56

[18] Blöchl P E 1994 Projector-augmented wave method *Phys. Rev.* B **50** 17953

[19] Kresse G and Joubert D 1999 From ultrasoft pseudopotentials to the projector augmented-wave method *Phys. Rev.* B **59** 1758–75

[20] Torrent M, Jollet F, Bottin F, Zérah G and Gonze X 2008 Implementation of the projector-augmented wave method in the abinit code: application to the study of iron under pressure *Comput. Mater. Sci.* **42** 337–51

[21] Gonze X *et al* 2002 First-principles computation of material properties: the ABINIT software project *Comput. Mater. Sci.* **25** 478–92

[22] Holzwarth N A W, Tackett A R and Matthews G E 2001 A projector augmented wave (PAW) code for electronic structure calculations, Part I: *atompaw* for generating atom-centered functions *Comput. Phys. Commun.* **135** 329–47

[23] Perdew J P, Burke K and Ernzerhof M 1996 Generalized gradient approximation made simple *Phys. Rev. Lett.* **77** 3865–8

[24] Monkhorst H J and Pack J D 1976 Special points for Brillouin-zone integrations *Phys. Rev.* B **13** 5188–92

[25] Czjzek G, Ford J L C, Love J C, Obenshain F E and Wegener H H F 1968 Coulomb-recoil-implantation Mössbauer experiments with ^{73}Ge *Phys. Rev.* **174** 331–45

[26] Zimmermann B H, Jena H, Ischenko G, Kilian H and Seyboth D 1968 Mössbauer experiments with Coulomb-excited ^{73}Ge after Coulomb recoil implantation *Phys. Status Solidi* **27** 639

[27] Potzel W 1993 Zinc-67 Mössbauer spectroscopy *Mössbauer Spectroscopy Applied to Magnetism and Materials Science* vol 1, ed G J Long and F Grandjean (New York: Plenum) pp 305–71

[28] Gonze X C 1997 First-principles responses of solids to atomic displacements and homogeneous electric fields: implementation of a conjugate gradient algorithm *Phys. Rev.* B **55** 10337–54

[29] Gonze X C and Lee C 1997 Dynamical matrices, Born effective charges, dielectric permittivity tensors and interatomic force constants from density-functional perturbation theory *Phys. Rev.* B **55** 10355–68

[30] Buheitel F, Potzel W and Aumann D C 1989 Calibration of isomer shifts of the 93.3 keV resonance in ^{67}Zn *Hyperfine Interact.* **47/48** 606

[31] Desgreniers S 1998 High-density phases of ZnO: structural and compressive parameters *Phys. Rev.* B **58** 14102–5

[32] Karzel H *et al* 1992 High-pressure phase transition in ^{67}ZnO *Hyperfine Interact.* **70** 1067–70

[33] Mori Y, Niiya N, Ukegawa K, Mizuno T, Takarabe K and Ruoff A L 2004 High-pressure x-ray structural study of BeO and ZnO to 200 GPa *Phys. Status Solidi* b **241** 3198–202

[34] Schulz H and Thiemann K H 1979 Structure parameters and polarity of the wurtzite-type compounds *Solid State Commun.* **32** 783–5

[35] Sawada H, Wang R P and Sleight A W 1996 An electron density residual study of zinc oxide *J. Solid State Chem.* **122** 148–50

[36] Pyykkö P 2008 Year-2008 nuclear quadrupole moments *Mol. Phys.* **106** 1965–74